PHYSICAL REVIEW B **109**, 085411 (2024)

Enhancement and anisotropy of electron Landé factor due to spin-orbit interaction in semiconductor nanowires

Julian Czarnecki,[1,*] Andrea Bertoni,[2,†] Guido Goldoni,[3,2,‡] and Paweł Wójcik[1,§]
[1]*AGH University of Krakow, Faculty of Physics and Applied Computer Science, al. A. Mickiewicza 30, 30-059 Krakow, Poland*
[2]*CNR-NANO S3, Istituto Nanoscienze, Via Campi 213/a, 41125 Modena, Italy*
[3]*Department of Physics, Informatics and Mathematics, University of Modena and Reggio Emilia, via Campi 213/a, 41125 Modena, Italy*

(Received 11 July 2023; revised 11 December 2023; accepted 17 January 2024; published 12 February 2024)

We investigate the effective Landé factor in semiconductor nanowires with strong Rashba spin-orbit coupling. Using the $\mathbf{k}\cdot\mathbf{p}$ theory and the envelope function approach we derive a conduction band Hamiltonian where g^* is explicitly related to the spin-orbit coupling constants $\boldsymbol{\alpha}_R$. Our model includes orbital effects from the Rashba spin-orbit term, leading to a significant enhancement of the effective Landé factor which is naturally anisotropic. For nanowires based on the low-gap, high spin-orbit coupled material InSb, we investigate the anisotropy of the effective Landé factor with respect to the magnetic field direction, exposing a twofold symmetry for the bottom gate architecture. The anisotropy results from the competition between the localization of the envelope function and the spin polarization of the electronic state, both determined by the magnetic field direction.

DOI: 10.1103/PhysRevB.109.085411

I. INTRODUCTION

Semiconductor nanowires (NWs) continue to attract significant interest due to the abundance of physical phenomena observed in such nanostructures, as well as the wealth of potential applications, including optoelectronics [1–4], quantum computing [5–7], or spintronics [8–11]. Applications in spintronics are largely driven by the spin-orbit (SO) interaction, which—in low energy gap semiconductors, such as InAs or InSb—is sufficiently strong to enable electrical control of the electron spin. In general, the SO interaction originates from the lack of the inversion symmetry, which could be an intrinsic feature of the crystallographic structure (Dresselhaus SO coupling [12]) or induced by the asymmetry of the confinement potential (Rashba SO coupling [13]). The latter has the essential advantage of being tunable by external fields, e.g., using gates attached to the nanostructures, as predicted theoretically [14–21] and demonstrated in recent experiments [22–26].

The significant progress in heteroepitaxy, which has been made over the last decade, enables the growth of a thin superconducting layer on the surface of semiconductor [27–30]. In this respect, hybrid NWs with a large SO interaction are recently intensively studied as the basic building blocks for topological quantum computing based on Majorana zero modes [31–35]. These exotic states are formed at the ends of NWs when the system becomes spinless, which is achieved in experiments by applying a magnetic field and the corresponding spin Zeeman effect [31]. The induced topological gap strongly depends on the strength of the SO coupling and the energy of the Zeeman splitting [36–38], usually expressed in terms of a linear response to the magnetic field with a proportionality constant g^*—the effective Landé factor. In other words, g^* determines the strength of the magnetic field required to trigger the system into the topological phase. For this reason, it is desirable to make it as large as possible, as the magnetic field needed for the topological transition is required to be lower than the critical magnetic field of the superconducting shell [33].

In semiconducting materials g^* is significantly different from the free-electron Landé factor g_0, due to coupling between the valence and the conduction band. In the second-order perturbation $\mathbf{k}\cdot\mathbf{p}$ theory it leads to the Roth-Lax-Zwerdling (RLZ) formula [39], which for low gap semiconductors gives $g^* \ll g_0$, e.g., $g^* \approx -49$ for InSb. In particular, for semiconductor nanostructures the RLZ formula predicts *a reduction* of the effective Landé factor with respect to the bulk value [40–42], as the subband confinement increases the energy gap, which is inversely proportional to g^* [39]. However, unexpectedly, recent experiments in NWs based on InAs and InSb exhibit opposite behavior—the extracted g^* is up to three times larger than the bulk value [7,43,44]. Furthermore, in Ref. [44], a step like evolution of g^* has been reported as a function of the gate voltage. It has been recently proposed that this surprising behavior arises from the $\mathbf{L}\cdot\mathbf{S}$ coupling, which for higher subbands (characterized by the large orbital momentum) leads to the enhancement of g^* by about one order of magnitude [45].

In this paper, we develop a full 8×8 $\mathbf{k}\cdot\mathbf{p}$ theory of the effective Landé factor in semiconductor NWs which takes into account the orbital effects in the SO coupling terms induced by an external magnetic field of arbitrary direction. For a nanowire based on the low-gap, strongly SO coupled material InSb, we performed fully self-consistent calculations taking

---

[*] jczarnecki@student.agh.edu.pl
[†] andrea.bertoni@nano.cnr.it
[‡] guido.goldoni@unimore.it
[§] pawel.wojcik@fis.agh.edu.pl

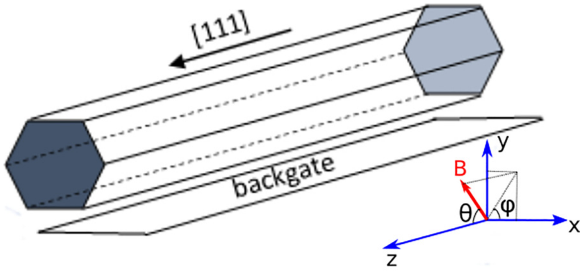

FIG. 1. Schematic illustration of a NW with a bottom gate together with a coordinate system with the magnetic field direction determined by two angles θ and φ.

into account on equal footing orbital and Zeeman effects of the applied magnetic field, SO coupling and the electrostatic environment. We demonstrate that the orbital contribution to g^* ensuing from the SO interaction may overcome the bulk contribution, leading to the enhancement of the effective Landé factor by an order of magnitude, even for the lowest subband, the one usually considered in Majorana experiments. Finally, we also evaluate the anisotropy of the SO-induced Landé factor with respect to the magnetic field rotated in different planes. Our results qualitatively agree with recent experiments [7,43,44] reproducing the enhancement of g^* and its anisotropy.

The paper is organized as follows. In Sec. II A, the Landé factor is derived from the $8 \times 8\,\mathbf{k}\cdot\mathbf{p}$ model within the envelope function approximation. Details on the numerical method are given in Sec. II B. Section III contains results of our calculations for homogeneous InSb NWs and their discussion with respect to recent experiments. Section IV summarizes our results.

II. THEORETICAL MODEL

Below we shall derive a $\mathbf{k}\cdot\mathbf{p}$ formulation of the Landé factor in semiconductor NWs. We shall specifically consider a homogeneous InSb, with hexagonal cross section, grown in the zincblede crystallographic structure along the [111] direction. This particular orientation preserves the crystal inversion symmetry, resulting in the reduction of the Dresselhaus SO coupling term [12,22].

The system is subjected to a uniform external magnetic field with intensity B. The direction of the applied magnetic field with respect to the NW axis is determined by the angles θ, between the field and the NW axis (z), and φ, between the x axis (oriented along the corner-corner direction) and the projection of the field on the xy plane—see Fig. 1. Hence,

$$\begin{aligned}\mathbf{B} &= [B_x, B_y, B_z]^T\\ &= B[\sin(\theta)\cos(\varphi), \sin(\theta)\sin(\varphi), \cos(\theta)]^T.\end{aligned} \tag{1}$$

We adopt the symmetric vector potential

$$\mathbf{A}(\mathbf{r}) = \left[-\frac{yB_z}{2}, \frac{xB_z}{2}, yB_x - xB_y\right]^T \tag{2}$$

and assume that the back gate is attached directly to the bottom facet of NW, generating an electric field in the xy plane. Although in real experiments a dielectric layer separating the NW from the gate is usually used, it plays a role of screening for the electric field. Hence, the value of the Landé factor obtained for a particular gate voltage V_g can be considered as the maximum achievable value at that specific V_g.

A. k · p theory of the Landé factor

Our model is based on the $8 \times 8\,\mathbf{k}\cdot\mathbf{p}$ approximation described by

$$\hat{\mathbf{H}}_{8\times8} = \begin{bmatrix}\hat{\mathbf{H}}_c & \hat{\mathbf{H}}_{cv}\\ \hat{\mathbf{H}}_{cv}^\dagger & \hat{\mathbf{H}}_v\end{bmatrix}, \tag{3}$$

where $\hat{\mathbf{H}}_c$ is the Hamiltonian of the conduction band electrons corresponding to the Γ_{6c} band. In the presence of the magnetic field $\hat{\mathbf{H}}_c$ can be written as

$$\hat{\mathbf{H}}_c = H_{\Gamma_{6c}}\mathbf{I}_{2\times2} + \tfrac{1}{2}\mu_B g_0 \boldsymbol{\sigma}\cdot\mathbf{B}, \tag{4}$$

where the second term corresponds to the Zeeman spin effect, μ_B is the Bohr magneton, g_0 is the Landé factor of the free electron and $\boldsymbol{\sigma} = (\sigma_x, \sigma_y, \sigma_z)$ is the vector of Pauli matrices, while

$$\hat{H}_{\Gamma_{6c}} = \frac{\hat{\mathbf{P}}^2}{2m_0} + E_c + V(\mathbf{r}), \tag{5}$$

where $\hat{\mathbf{P}} = \hat{\mathbf{p}} - e\mathbf{A}$, e is the electron charge, m_0 is the free electron mass and E_c is the conduction band minima. The potential $V(\mathbf{r})$ in (5) contains the interaction of electrons with the electric field generated by the external gates $V_g(\mathbf{r})$ and the electron-electron interaction included in our model at the mean-field level (Hartree potential) $V_H(\mathbf{r})$, $V(\mathbf{r}) = V_g(\mathbf{r}) + V_H(\mathbf{r})$.

Below we shall use a folding procedure of $\hat{\mathbf{H}}_{8\times8}$ to the conduction band sector, where in the Hamiltonian $\hat{\mathbf{H}}_v$, related to valance bands Γ_{8v} and Γ_{7v}, all off-diagonal elements are neglected. Then, $\hat{\mathbf{H}}_v$ can be written as

$$\hat{\mathbf{H}}_v = H_{\Gamma_{8v}}\mathbf{I}_{4\times4} \oplus H_{\Gamma_{7v}}\mathbf{I}_{2\times2}, \tag{6}$$

with

$$\begin{aligned}H_{\Gamma_{7v}} &= E_{v'} = E_c + V(\mathbf{r}) - E_0 - \Delta_0,\\ H_{\Gamma_{8v}} &= E_v = E_c + V(\mathbf{r}) - E_0,\end{aligned} \tag{7}$$

where E_0 is the energy gap and Δ_0 is the energy of SO splitting in the valence band. Note that Eq. (6) neglects the kinetic term and Zeeman splitting in the valance band as the corresponding energies are much smaller than E_0 and Δ_0.

The coupling between the conduction band and the valence band is described by the off-diagonal matrix $\hat{\mathbf{H}}_{cv}$,

$$\hat{\mathbf{H}}_{cv} = \frac{P_0}{\hbar}\begin{bmatrix}\frac{\hat{P}_+}{\sqrt{6}} & 0 & \frac{\hat{P}_-}{\sqrt{2}} & -\frac{\sqrt{2}\hat{P}_z}{\sqrt{3}} & -\frac{\hat{P}_z}{\sqrt{3}} & \frac{\hat{P}_+}{\sqrt{3}}\\ -\frac{\sqrt{2}\hat{P}_z}{\sqrt{3}} & -\frac{\hat{P}_+}{\sqrt{2}} & 0 & -\frac{\hat{P}_-}{\sqrt{6}} & \frac{\hat{P}_-}{\sqrt{3}} & \frac{\hat{P}_z}{\sqrt{3}}\end{bmatrix}, \tag{8}$$

where $\hat{P}_\pm = \hat{P}_x \pm i\hat{P}_y$ and the parameter $P_0 = \frac{-i\hbar}{m_0}\langle S|\hat{p}_x|X\rangle$ accounts for the coupling between conduction and valence bands at the Γ point of the Brillouin zone.

Using the standard folding-down transformation, we can reduce the $8 \times 8\ \mathbf{k}\cdot\mathbf{p}$ model (3) into the effective 2×2

Hamiltonian for conduction electrons

$$\hat{\mathbf{H}}_{\text{eff}} = \hat{\mathbf{H}}_c - \hat{\mathbf{H}}_{cv}(\hat{\mathbf{H}}_v - E)^{-1}\hat{\mathbf{H}}_{cv}^{\dagger} = \hat{\mathbf{H}}_c + \tilde{\mathbf{H}}_c. \tag{9}$$

In the above formula, $\tilde{\mathbf{H}}_c$ can be written in terms of Pauli matrices

$$\tilde{\mathbf{H}}_c = \lambda_0 \mathbf{I}_{2\times 2} + \boldsymbol{\lambda}\cdot\boldsymbol{\sigma}, \tag{10}$$

where

$$\lambda_0 = \frac{P_0^2}{3\hbar^2}\left[\hat{P}_x\left(\frac{2}{E_v - E} + \frac{1}{E_{v'} - E}\right)\hat{P}_x + \hat{P}_y\left(\frac{2}{E_v - E} + \frac{1}{E_{v'} - E}\right)\hat{P}_y\right], \tag{11a}$$

$$\lambda_x = \frac{iP_0^2}{3\hbar^2}\left[\hat{P}_z\left(\frac{1}{E_v - E} - \frac{1}{E_{v'} - E}\right)\hat{P}_y - \hat{P}_y\left(\frac{1}{E_v - E} - \frac{1}{E_{v'} - E}\right)\hat{P}_z\right], \tag{11b}$$

$$\lambda_y = \frac{iP_0^2}{3\hbar^2}\left[\hat{P}_x\left(\frac{1}{E_v - E} - \frac{1}{E_{v'} - E}\right)\hat{P}_z - \hat{P}_z\left(\frac{1}{E_v - E} - \frac{1}{E_{v'} - E}\right)\hat{P}_x\right], \tag{11c}$$

$$\lambda_z = \frac{iP_0^2}{3\hbar^2}\left[\hat{P}_y\left(\frac{1}{E_v - E} - \frac{1}{E_{v'} - E}\right)\hat{P}_x - \hat{P}_x\left(\frac{1}{E_v - E} - \frac{1}{E_{v'} - E}\right)\hat{P}_y\right]. \tag{11d}$$

The first term in Eq. (10) leads to the standard formula for the effective mass

$$\frac{1}{m^*} = \frac{1}{m_0} + \frac{2P_0^2}{3\hbar^2}\left(\frac{2}{E_v} + \frac{1}{E_{v'}}\right), \tag{12}$$

while the second term corresponds to the Rashba SO coupling. If we assume that E_0 and Δ_0 are the largest energies in the system we can expand $E_{v(v')}$ in Eqs. (11b)–(11d) to the second order in energy. Then, Eqs. (11b)–(11d) can be rewritten as

$$\lambda_x = -\alpha_R^y\left(k_z - \frac{e}{\hbar}A_z\right) - \frac{eP_0^2}{3\hbar}\left(\frac{1}{E_0} - \frac{1}{E_0 + \Delta_0}\right)B_x, \tag{13a}$$

$$\lambda_y = \alpha_R^x\left(k_z - \frac{e}{\hbar}A_z\right) - \frac{eP_0^2}{3\hbar}\left(\frac{1}{E_0} - \frac{1}{E_0 + \Delta_0}\right)B_y, \tag{13b}$$

$$\lambda_z = \alpha_R^y\left(\hat{k}_x - \frac{e}{\hbar}A_x\right) - \alpha_R^x\left(\hat{k}_y - \frac{e}{\hbar}A_y\right) - \frac{eP_0^2}{3\hbar}\left(\frac{1}{E_0} - \frac{1}{E_0 + \Delta_0}\right)B_z, \tag{13c}$$

where

$$\boldsymbol{\alpha}_R = \left(\alpha_R^x, \alpha_R^y, \alpha_R^z\right) = \frac{P_0^2}{3}\left(\frac{1}{E_0^2} - \frac{1}{(E_0 + \Delta_0)^2}\right)\nabla V(x, y) \tag{14}$$

is the Rashba SO coupling constant and we assume $\hat{p} = \hbar(\hat{k}_x, \hat{k}_y, k_z) = \hbar(-i\partial/\partial x, -i\partial/\partial y, k_z)$. Note that in Eqs. (13a) and (13b), we have already omitted α_R^z terms since the magnetic field does not break translational invariance along the wire axis, i.e.,

$$\Psi_{n,k_z}(x, y, z) = \psi_{n,k_z}(x, y)e^{ik_z z} = \left[\psi_{n,k_z}^{\uparrow}(x, y), \psi_{n,k_z}^{\downarrow}(x, y)\right]^T e^{ik_z z}. \tag{15}$$

From $\hat{\mathbf{H}}_{\text{eff}}$, we determine the spin-split energy subbands $E_{n,k_z}(\mathbf{B})$, and from these the effective g^* factor of the lowest state as

$$g^* = \frac{(E_{2,kz}(\mathbf{B}) - E_{2,kz}(0)) - (E_{1,kz}(\mathbf{B}) - E_{1,kz}(0))}{\mu_b \hbar B}. \tag{16}$$

Note that the above definion of g^* excludes the spin splitting which is due to the SO coupling solely, and may be present also at $B = 0$ (at which $g^* = 0$). However, the total SO term involves the magnetic field by the kinetic momentum, and it also contributes to the effective Landé factor. To show that, let us decompose the SO term into the part depending on the canonical momentum $\mathbf{k}$ and the vector potential, $\mathbf{A}$. Then, the effective Hamiltonian for conduction electrons can be written as

$$\hat{\mathbf{H}}_{\text{eff}} = \left(\frac{\hat{\mathbf{P}}^2}{2m^*} + E_c + V(\mathbf{r})\right)\mathbf{I}_{2\times 2} + \left(\alpha_R^x\sigma_y - \alpha_R^y\sigma_x\right)k_z + \left(\alpha_R^y\hat{k}_x - \alpha_R^x\hat{k}_y\right)\sigma_z + \frac{1}{2}\mu_B\mathbf{B}\mathbf{g}^*\boldsymbol{\sigma} \tag{17}$$

where $\mathbf{g}^*$ is a tensor given by

$$\mathbf{g}^* = g_{\text{RLZ}}\mathbf{I}_{3\times 3} + \mathbf{g}_{\text{SO}}, \tag{18}$$

and

$$g_{\text{RLZ}} = g_0 - \frac{2E_p}{3}\left(\frac{1}{E_0} - \frac{1}{E_0 + \Delta_0}\right), \tag{19}$$

which corresponds to the well-know RLZ formula [39] ($E_p = 2m_0P_0^2/\hbar^2$), while the tensor $\mathbf{g}_{\text{SO}}$ results from the orbital effects of the magnetic field in the SO Hamiltonian,

$$\mathbf{g}_{\text{SO}} = \begin{bmatrix} g_{\text{SO}}^{xx} & g_{\text{SO}}^{xy} & 0 \\ g_{\text{SO}}^{yx} & g_{\text{SO}}^{yy} & 0 \\ 0 & 0 & g_{\text{SO}}^{zz} \end{bmatrix}. \tag{20}$$

Using the vector potential (2), the elements of this tensor can be expressed as

$$g_{\text{SO}}^{xx} = \frac{2e}{\mu_B\hbar}\alpha_R^y y, \tag{21a}$$

$$g_{\text{SO}}^{yy} = \frac{2e}{\mu_B\hbar}\alpha_R^x x, \tag{21b}$$

$$g_{\text{SO}}^{zz} = \frac{e}{\mu_B\hbar}\left(\alpha_R^y y - \alpha_R^x x\right), \tag{21c}$$

$$g_{\text{SO}}^{xy} = -\frac{2e}{\mu_B\hbar}\alpha_R^x y, \tag{21d}$$

$$g_{\text{SO}}^{yx} = -\frac{2e}{\mu_B\hbar}\alpha_R^y x, \tag{21e}$$

which shows that $\mathbf{g}^*$ depends linearly on the vector of Rashba SO coupling constants $\boldsymbol{\alpha}_R$.

Note that $\mathbf{g}_{\text{SO}}$ is not an observable and it is gauge dependent (while of course $\lambda_x(y, z)$ in Eqs. (13a)–(13c), hence g^*, are gauge invariant, as they involve the kinetic momentum P).

However, since it explicitly demonstrates the contribution to the effective Landé factor from the SO coupling, it is useful to use $\mathbf{g}_{\mathrm{SO}}$ for analyzing g^*.

Since the Rashba coefficients and the SO induced Landé factor are functions of space [see Eqs. (14) and (21)], we discuss the matrix elements of the Rashba SO coupling constants

$$\left\langle \alpha_R^{x(y)}(k_z)\right\rangle_n = \langle \psi_{n,k_z}|\alpha_R^{x(y)}\sigma_{y(x)}|\psi_{n,k_z}\rangle \tag{22}$$

and the individual diagonal and off-diagonal matrix elements of $\mathbf{g}_{\mathrm{SO}}$, respectively defined as

$$\left\langle g_{\mathrm{SO}}^{xx(yy,zz)}(k_z)\right\rangle_n = \langle \psi_{n,k_z}|g_{\mathrm{SO}}^{xx(yy,zz)}\sigma_{x(y,z)}|\psi_{n,k_z}\rangle, \tag{23a}$$

$$\left\langle g_{\mathrm{SO}}^{xy(yx)}(k_z)\right\rangle_n = \langle \psi_{n,k_z}|g_{\mathrm{SO}}^{xy(yx)}\sigma_{y(x)}|\psi_{n,k_z}\rangle, \tag{23b}$$

where $|\psi_{n,k_z}\rangle$ is the in-plane part of the n-th envelope functions of NW, to be calculated as described in the following section.

It is useful to compare our derivation with Lassnig's for the two dimensional gas, reported in Ref. [46]. There, g^* has been defined in such a way that its first derivative determines the SO coupling constant, hence it contains information about the *total* spin splitting of the energy levels, ensuing both from the linear Zeeman term and the SO coupling, whose dependence on the magnetic field is more complex. Here, instead, we define the effective Landé factor as the coefficient of proportionality between the spin splitting of the energy levels induced by the external magnetic field and the magnitude of the field. This procedure allows to distinguish between two effects among which the one which changes with $\mathbf{B}$ defines the effective Landé factor. Note that such a definition is usually used in experiments to determine g^* [7,43,44].

B. Numerical calculations

To understand the physics behind the behavior of the Landé factor in NWs with strong SO coupling, we use a numerical approach taking into account important key ingredients, namely the orbital and Zeeman effect, SO coupling and electrostatic environment. For this purpose, we employ a standard Shrödinger-Poisson approach [17,18,47–51]. Assuming the translational invariance along the growth axis z, the envelope functions $\psi_{n,k_z}(x,y) = [\psi_{n,k_z}^{\uparrow}(x,y), \psi_{n,k_z}^{\downarrow}(x,y)]$ can be determined from the Schrödinger equation

$$\begin{aligned}&\bigg[\bigg(\frac{\hat{\mathbf{P}}_{2D}^2}{2m^*} + \frac{1}{2}m^*\omega_c^2\big[(y\cos\theta - x\sin\theta)\sin\varphi - k_z l_B^2\big]^2 + E_c\\ &+ V(\mathbf{r})\bigg)\mathbf{I}_{2\times 2} + \big(\alpha_R^x\sigma_y - \alpha_R^y\sigma_x\big)k_z + \big(\alpha_R^y\hat{k}_x - \alpha_R^x\hat{k}_y\big)\sigma_z\\ &+ \frac{1}{2}\mu_B\mathbf{B}\mathbf{g}^*\boldsymbol{\sigma}\bigg]\psi_{n,k_z}(x,y) = E_{n,k_z}\psi_{n,k_z}(x,y),\end{aligned} \tag{24}$$

where $\alpha_R^{x(y)}$ and $\mathbf{g}^*$ are functions of the position (x, y), $\omega_c = eB/m^*$ is the cyclotron frequency, $l_B = \sqrt{\hbar/eB}$ is the magnetic length and

$$\hat{\mathbf{P}}_{2D}^2 = \left(\hat{p}_x + eB\frac{y\cos\varphi}{2}\right)^2 + \left(\hat{p}_y - eB\frac{x\cos\varphi}{2}\right)^2. \tag{25}$$

Note that in the presence of magnetic field and SO coupling the Hamiltonian (24) depends on the k_z vector. The calculations are carried out on a uniform grid in the range $[-k_z^{\max}, k_z^{\max}]$ where $k_z^{\max}$ is chosen to be much larger than the Fermi wave vector. The term $(\alpha_R^y\hat{k}_x - \alpha_R^x\hat{k}_y)\sigma_z$ in Hamilonian (24) needs an additional comment as it may suggest the violation of time reversal symmetry. As we checked, this is not the case and $[(\alpha_R^y\hat{k}_x - \alpha_R^x\hat{k}_y)\sigma_z, \mathcal{T}] = 0$, where $\mathcal{T} = \mathcal{K}(-y\sigma_y)$ and $\mathcal{K}$ is the complex conjugate operator. As a result, at $\mathbf{B} = 0$ the Kramers degeneracy is preserved, resulting in the crossing of states at $k_z = 0$.

The self-consistent potential $V(\mathbf{r})$ in Eq. (24) is determined at the mean-field level by solving the Poisson equation

$$\nabla_{2D}^2 V(x,y) = -\frac{n_e(x,y)}{\epsilon_0\epsilon}, \tag{26}$$

where ϵ is a dielectric constant and the electron density n_e can be calculated based on the formula

$$n_e(x,y) = \sum_n \int_{-k_z^{\max}}^{k_z^{\max}} \frac{1}{2\pi}|\psi_{n,k_z}(x,y)|^2 f(E_{n,k_z} - \mu, T)dk_z \tag{27}$$

where μ is the chemical potential, T is the temperature and $f(E,T)$ is the Fermi-Dirac distribution.

In the applied Shrödinger-Poisson approach, Eqs. (24) and (26) are solved alternatively until the self-consistency is reached, which we consider to occur when the relative variation of the charge density between two consecutive iterations is lower than 0.001. In each iteration a spatial distribution of $\alpha_R^{x(y)}$ and g_{SO}^{ab}, where $a, b = \{x, y, z\}$, are determined based on Eqs. (14) and (21). Numerical calculations are carried on the triangular grid, which preserves the hexagonal symmetry of the Hamiltonian at zero field, avoiding artifacts such as spurious level splittings which may appear when using rectangular grid symmetry [47]. We assume Dirichlet boundary condition for all the facets with a specified condition for the bottom one, defined by the voltage applied to the gate. Finally, the energy spectrum E_{n,k_z}, the self-consistent potential $V(x,y)$ and the corresponding wave functions $\psi_{n,k_z}(x,y)$ are used to determine g^*, $\langle\alpha_R^{x,(y)}\rangle_n$ as well as $\langle g_{\mathrm{SO}}^{xx(yy,zz)}\rangle_n$ and $\langle g_{\mathrm{SO}}^{xy(yx)}\rangle_n$ tensor elements according to Eqs. (16), (22), and (23).

Calculations have been carried out for the material parameters corresponding to InSb: $E_0 = 0.235$ eV, $\Delta_0 = 0.81$ eV, $m^* = 0.014$, $E_P = \frac{2m_0P}{2} = 23.3$ eV, $T = 4.2$ K, and for the nanowire width $W = 100$ nm (corner-to-corner). We keep the constant linear electron density at the low level $n_e = 8 \times 10^7$ cm^{-1}, which guarantees that only the lowest subband is occupied in the range of the considered magnetic field $B = [0, 4]$ T.

III. RESULTS

We shall now discuss the effective Landé factor as a function of the magnetic field intensity and direction. As g_{RLZ} evaluated from the RLZ formula ($g_{\mathrm{RLZ}} = -49$ for the present material) does not depend on the magnetic field, we put particular emphasis on the role of the SO-induced component $\mathbf{g}_{\mathrm{SO}}$ in terms of the tensor elements, Eqs. (21). As shown in the previous section, corrections to the Landé factor coming from the SO interaction are indirectly dependent on the wave vector via ψ_{n,k_z}, which results from the orbital effects of the magnetic field. For this reason, we shall study both g^* and

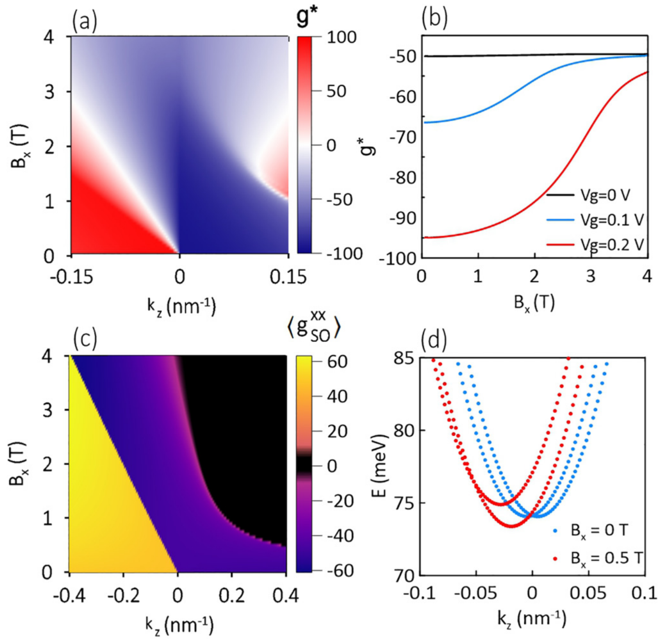

FIG. 2. (a) Map of g^* [Eq. (16)] as a function of wave vector k_z and magnetic field oriented along the x axis, B_x. (b) $g^*(B_x)$ calculated at $k_z = 0$ at selected V_g. (c) Map of $\langle g^{xx}_{\rm SO}\rangle$ as a function of wave vector k_z and magnetic field, B_x. (b) Dispersion relations without magnetic field (blue) and at $B_x = 0.5$ T (red). The shift of the crossing point on (d) corresponds to the sign change of $\langle g^{xx}_{\rm SO}\rangle$ in (c).

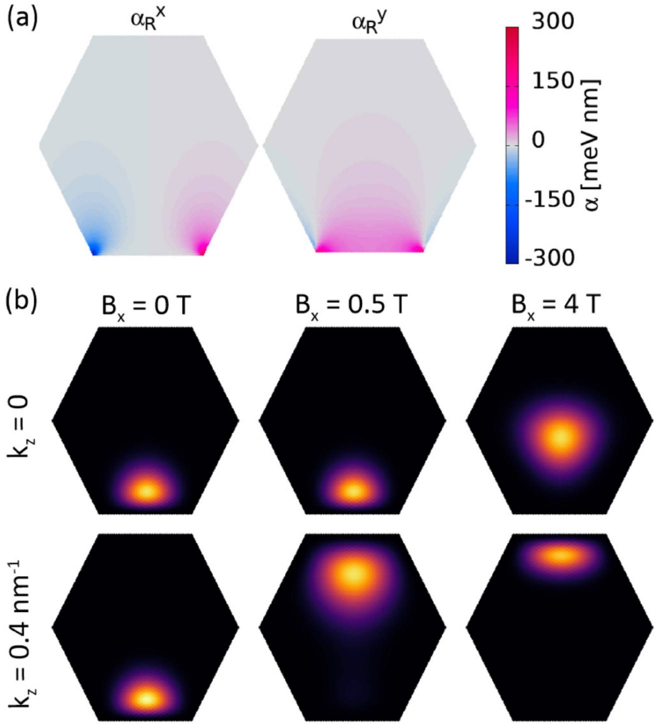

FIG. 3. (a) Map of the SO Rashba coefficients α_R^x, α_R^y. (b) Squared envelope functions of the lowest subband with the magnetic field oriented along x, at selected magnetic field intensity B_x and the wave vectors k_z.

$\mathbf{g}_{\rm SO}$ as a function of both the wave vector and the magnetic field. We limit our study to the lowest subband assuming the electrical potential is applied to the bottom gate to induce SO coupling. For simplicity, in the rest of the paper, we omit the subband index in Eqs. (22) and (23), i.e., $\langle \ldots \rangle_{n=1} = \langle \ldots \rangle$.

A. Enhancement of the Landé factor due to SO coupling

First, we show that a magnetic field oriented along the x axis, i.e., perpendicular to the NW axis *and* to the direction of $\langle \boldsymbol{\alpha}_R\rangle$, results in a substantial enhancement of the effective Landé factor. For this purpose, we assume that $V_g = 0.2$ V is applied to the bottom gate, generating an electric field that mantains reflection symmetry with respect to the y axis; hence $\langle \boldsymbol{\alpha}_R\rangle$ is directed along y by symmetry.

In Fig. 2(a), we show the effective Landé factor g^* [see Eq. (16)] vs k_z and B. In this configuration $|g^*|$ reaches values up to 100, twice as large as predicted from the RLZ formula ($g_{\rm RLZ} = -49$). The maximum of $|g^*|$ is determined by the gate voltage, as shown in Fig. 2(b) where we report the calculated $g^*(B_x)$ at $k_z = 0$ for selected values of V_g. Note that at $V_g = 0$, when the SO coupling is absent, $g^* = g_{\rm RLZ}$ which strongly suggests that the observed enhancement of the Landé factor is related to the orbital effects in the SO term. In order to show that, in Fig. 2(c), we present the map of the diagonal element $\langle g^{xx}_{\rm SO}\rangle(k_z, B_x)$. Note that with this field configuration the off-diagonal elements vanish by symmetry. Indeed, the reflection symmetry of the electric field with respect to the y axis leads to $\langle \alpha_R^x\rangle = 0$, hence $\langle g^{xy}_{\rm SO}\rangle = 0$ [see Eq. (21d)]. Moreover, the even symmetry of the envelope function is unaffected by the magnetic field directed along x, hence $\langle g^{yx}_{\rm SO}\rangle = 0$ [see Eqs. (21e)]. Figure 2(c) clearly demonstrates that the correction to the effective Landé factor arising from the orbital effects in the SO coupling term reaches a value similar to that obtained from the RLZ formula. Under certain conditions, this enhancement can lead to a significant increase of g^*, almost doubling it, as observed in recent experiments [7,43,44].

In Fig. 2(c), we distinguish three regions, with positive (yellow), negative (purple) and vanishing (black) $\langle g^{xx}_{\rm SO}\rangle$. The abrupt change of sign between positive and negative regions is simply understood as the crossing of subbands of opposite spin, since only the value for the lowest subband is shown here. Indeed, as shown in Fig. 2(d), the subband of opposite spin cross at $k_z = 0$ at vanishing field. When the field is switched on, both subband shift to negative k_z and shift in energy due to Zeeman term. Hence, the crossing shifts linearly with the field to more negative wave vectors, as shown in Fig. 2(c).

For sufficiently large $k_z > 0$ and field intensity, $\langle g^{xx}_{\rm SO}\rangle$ almost vanishes, as shown in Fig. 2(c) - black region. This can be explained by the analysis of the position-dependent SO coupling constants $\alpha_R^{x(y)}$ [see Eq. (14)] presented in the Fig. 3(a) at $B = 0$. Note that their spatial distribution is primarily influenced by the electric field generated by the bottom gate and do not undergo significant changes as the magnetic field increases. Since the value of $\mathbf{g}_{\rm SO}$ matrix elements depends on the Rashba SO coupling constant, the SO-induced modification of the Landé factor for a specific subband is most significant when its envelope function is localized in the regions of strong Rashba SO coupling. With this respect, the vanishing of $\langle g_{\mathrm{SO}}^{xx}\rangle$ in Fig. 2(c) is due to the change of the wave function localization, determined by the orbital coupling to the magnetic field.

In Fig. 3(b), we report the squared envelope functions of the lowest subbands at $k_z = 0$ and $k_z = 0.4\ \mathrm{nm}^{-1}$ at increasing magnetic fields. At $k_z = 0$ there is no kinetic coupling to the magnetic field and the localization of the envelope function is only determined by the electric field; hence, it concentrates near the bottom gate, where the SO coupling is strong. For a positive wave vectors k_z, instead, the orbital effects shift the wave function towards the opposite facet of the NW, where the SO coupling is weak, leading to vanishing $\langle g_{\mathrm{SO}}^{xx}\rangle$, which explains the black region in Fig. 2(c). As shown in Fig. 2(c), the stronger the magnetic field, the lower k_z is required to push the wave function away from the region with large SO coupling, near the bottom facet. Naively, one might expect that the state $k_z = 0$ would not be affected by this phenomenon as there is no orbital coupling to the magnetic field for this state. However, it should be noted that for high magnetic fields, diamagnetic effects become dominant, causing the wave functions to localize in the middle of NW along the field direction, resembling dispersionless Landau levels, as shown in Fig. 3(b). As the position of this wave function is associated with low SO coupling regions, $\langle g_{\mathrm{SO}}^{xx}\rangle$ gradually decreases towards zero, even for $k_z = 0$, as illustrated in Fig. 2(c). Thus, regardless of the gate voltage, g^* tends to approach g_{RLZ} when the magnetic field increases, see Fig. 2(b).

We next discuss the behavior of the effective Landé factor with the magnetic field directed either parallel to $\boldsymbol{\alpha}_R$ (along the y axis) or to the NW axis (along the z axis). When the magnetic field is applied parallel to $\boldsymbol{\alpha}_R$, $\langle g_{\mathrm{SO}}^{yy(yx)}\rangle \geqslant 0$, resulting in the increase of g^*. This is shown in Figs. 4(a) and 4(b). In this case, the deviation from g_{RLZ} is not as large as for the perpendicular orientation of $\mathbf{B}$—compare with Fig. 2(a). In this configuration the off-diagonal element $\langle g_{\mathrm{SO}}^{yx}\rangle$ is non-negligible, in contrast to $\langle g_{\mathrm{SO}}^{xy}\rangle$ which is nearly zero, as the average value of α_R^x is vanishing due to the gate symmetry. Again, the evolution of both $\langle g_{\mathrm{SO}}^{yy}\rangle$ and $\langle g_{\mathrm{SO}}^{yx}\rangle$ as a function of the magnetic field, shown in Figs. 4(c) and 4(d), respectively, is determined by the localization and symmetry of the wave function, whereas we assume the rule that we display only these tensor elements which contribute to the spin splitting for a particular field direction.

In Fig. 4(e), one can observe that at zero magnetic field, the wave function sets itself at the center-bottom of the NW. In this region, α_R^x is antisymmetric with respect to the x axis, resulting in the $\langle g_{\mathrm{SO}}^{yy}\rangle = \langle g_{\mathrm{SO}}^{yx}\rangle = 0$. The symmetry of the wave function is broken by the magnetic field, as depicted in Fig. 4(e). For $k_z = 0.4\ \mathrm{nm}^{-1}$, for increasing magnetic fields, the wave function is first localized at the bottom-left corner, where the contribution from negative α_R^x leads to nonzero values of $\langle g_{\mathrm{SO}}^{yy(yx)}\rangle$, and eventually in the left corner, where α_R^x is significantly lower, resulting in a decrease in $\langle g_{\mathrm{SO}}^{yy(yx)}\rangle$. This field-induced evolution leads to the maximum of $\langle g_{\mathrm{SO}}^{yy(yx)}\rangle$ at a certain k_z value, as illustrated in Figs. 4(c) and 4(d).

We next consider a magnetic field applied in z direction, i.e., along the NW axis. Decrease of $|g^*|$, shown in Fig. 5, has a different nature, since the orbital effects of magnetic field are

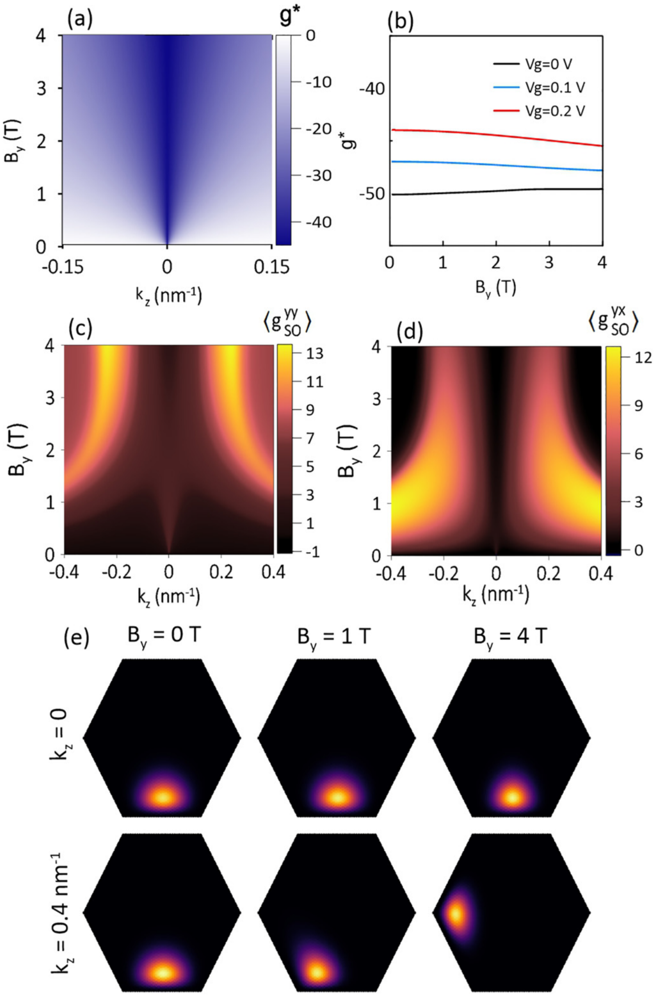

FIG. 4. (a) Map of g^* [Eq. (16)] as a function of wave vector k_z and magnetic field oriented along the y axis, B_y. (b) $g^*(B_y)$ calculated at $k_z = 0$. (c),(d) Diagonal $\langle g_{\mathrm{SO}}^{yy}\rangle$ and off-diagonal $\langle g_{\mathrm{SO}}^{yx}\rangle$ elements of $\mathbf{g}_{\mathrm{SO}}$ with the field oriented along y, as a function of wave vector k_z and field intensity B_y. (e) Squared envelope functions of the lowest energy state at selected different magnetic field intensity B_y and the wave vectors k_z.

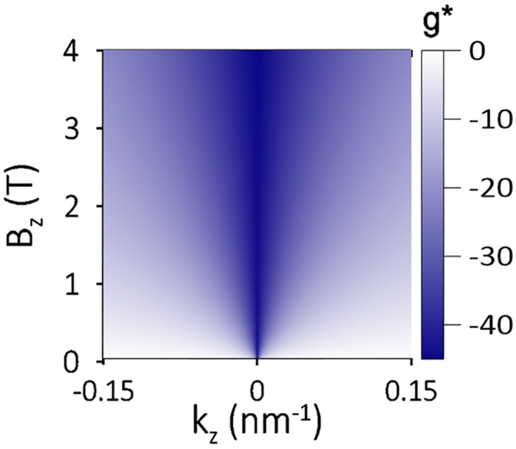

FIG. 5. Effective Landé factor g^* as a function of wave vector k_z and magnetic field magnitude oriented in the z direction, B_z.

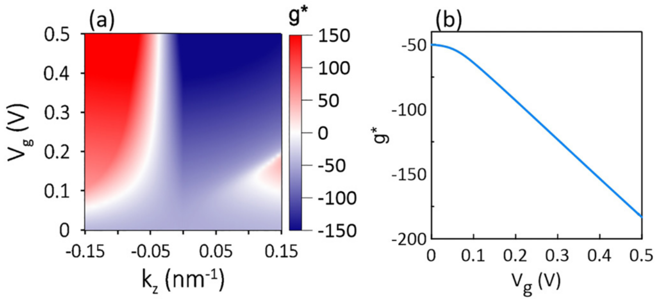

FIG. 6. (a) g^* as a function of wave vector k_z and bottom gate voltage V_g and (b) $g^*(V_g)$ at $k_z = 0$. Results for magnetic field directed along the x axis with $B_x = 1$ T.

highly reduced by the confinement. In this case the localization of the wave function is not measurably changed with the magnetic field, regardless of k_z, and thus it does not determine the evolution of g^* with k_z and B_z. In this configuration g^* is rather governed by the interplay between the Zeeman effect, which favors in-wire z polarization, and the SO interaction, which favors orthogonal polarization along y. Note that both the tensor element $\langle g^{zz}_{\mathrm{SO}} \rangle$ [see Eqs. (23)] and the total g^* factor, are defined by the energy splitting which depends on σ_z and thus to the relative distribution of spin up and down component in the spinor. Since the SO coupling depends on the wave vector, for a small k_z the ordinary Zeeman effect is dominant, aligning the electron spin along the magnetic field direction and—in the limit of $k_z = 0$—makes the system spin polarized along the z axis. The expectation value of σ_z in this case is the largest in the sense of absolute value, resulting in the large value of g^*. In other words, the value of g^* for small k_z results from the finite Rashba couplings near the bottom gate, where the wave function is localized and the almost complete z-spin polarization of electrons induced by the magnetic field. As a consequence, g^* is independent of the magnetic field magnitude at $k_z = 0$ (not shown here).

On the other hand, for a large value of k_z and low magnetic field, the SO coupling plays a major role, forcing the electron spin to align along the effective Rashba field directed in the x axis. In this scenario, the spin-up and spin-down components of the spinor become almost equal, resulting in a decrease in g^*. It is worth noting that even for a large k_z and strong SO coupling, an increasing magnetic field can deviate the electron spin direction from the x towards the z axis, leading to an overall increase in g^* with the magnetic field, as depicted in Fig. 5.

Finally, note that results presented in Fig. 5 for the magnetic field directed along the z axis at $k_z = 0$ corresponds to the physical situation considered theoretically in Ref. [45], where the enhancement of the effective Landé factor has been recently predicted in semiconductor NWs. The predicted effect was however restricted to the higher subbands characterized by the nonzero orbital momentum where the orbital effects are relevant. Here, we show that the enhancement of g^* for the lowest band is possible only when the magnetic field is applied perpendicular to $\boldsymbol{\alpha}_R$—in our setup along the x axis.

To summarize this section, in Fig. 6, we show the gate voltage dependence of g^*, calculated for a magnetic field directed along the x axis with $B_x = 1$ T. It can be observed that the inclusion of the SO effects may lead to a substantial increase of the effective Landé factor g^*, reaching up to four times the value obtained from the RLZ formula.

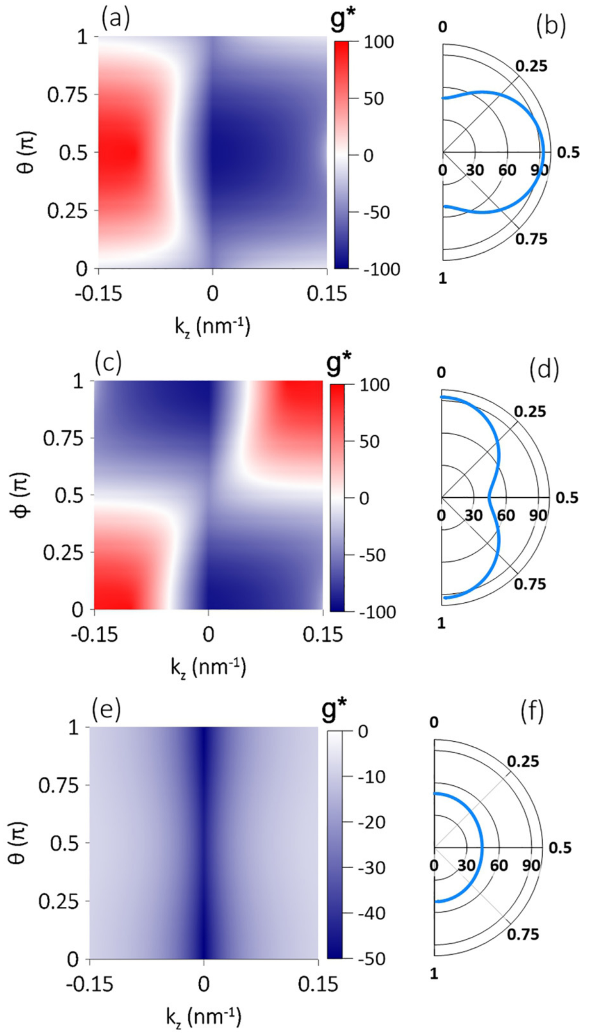

FIG. 7. Maps of g^* [Eq. (16)] as a function of wave vector k_z and magnetic field orientation when it is rotated [(a) and (b)] in the xz plane; [(c) and (d)] in the xy plane; [(e) and (f)] in the yz plane. Right polar plots present g^* evaluated at $k_z = 0$. Results for $B = 1$ T and $V_g = 0.2$ V.

B. Spin-orbital induced Landé factor anisotropy

We next analyze the anisotropy of g^* with respect to the field direction. For this purpose we consider a magnetic field with intensity $B = 1$ T rotated in (i) the xz plane ($\varphi = 0$), (ii) the xy plane ($\theta = \pi/2$), and (iii) the yz plane ($\varphi = \pi/2$). To induce Rashba SO coupling, we apply a gate voltage $V_g = 0.2$ V.

Figure 7 shows maps of g^* as a function of the wave vector k_z and the rotation angle for three considered rotation plane of the magnetic field. The effective Landé factor g^* determined at $k_z = 0$—see right polar plots in Fig. 7—exhibits the two fold anisotropy when the magnetic field is rotated in the xz and xy planes with the maximal value twice larger than g_{RLZ}

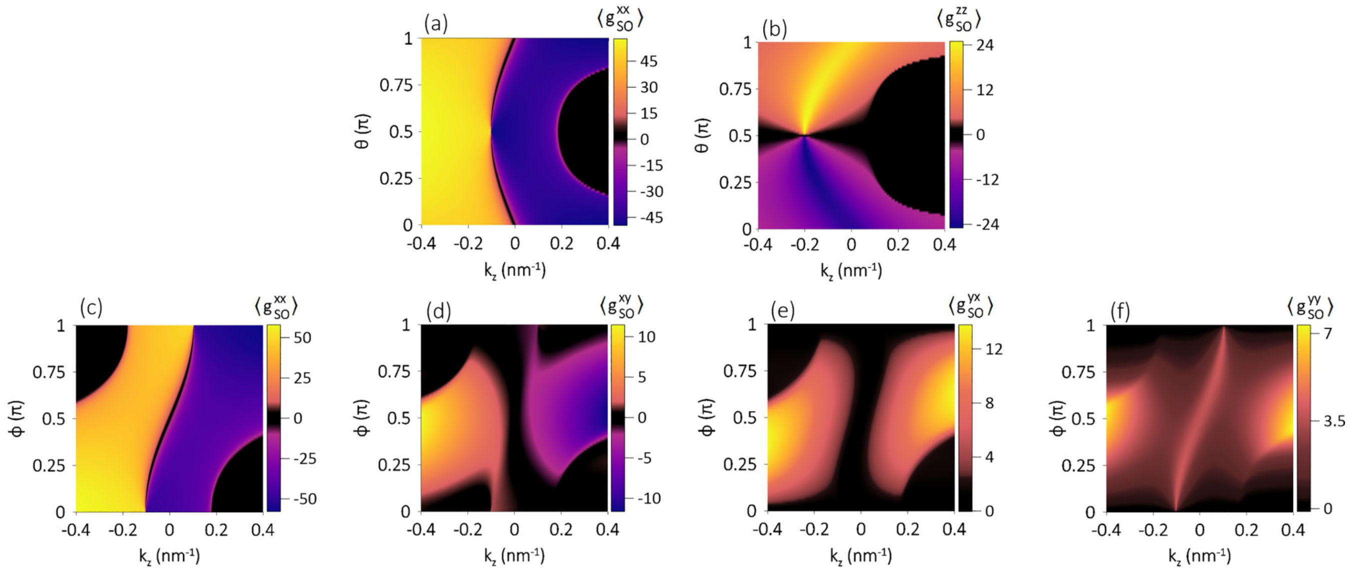

FIG. 8. Maps of tensor elements $\langle g_{\rm SO}^{ab}\rangle$ $(a, b = \{x, y, z\})$ as a function of wave vector k_z and magnetic field orientation when it is rotated [(a) and (b)] in the xz plane and [(c)–(f)] in the xy plane. Results for $B = 1$ T and $V_g = 0.2$ V.

for the magnetic field aligned along the x axis. The rotation in yz plane does not significantly change g^* exhibiting nearly isotropic behavior. Similarly, as in the previous section, the observed anisotropy can be explained as a combination of two phenomena: (i) the orbital effects coming from the SO term and (ii) the polarization of the spin state being a resultant of the Rashba SO coupling and the magnetic field.

To get into details of the orbital contribution coming from SO coupling in Figs. 8(a) and 8(b), we show maps of $\langle g_{\rm SO}^{xx}\rangle$ and $\langle g_{\rm SO}^{zz}\rangle$ as a function of the wave vector k_z and θ when the magnetic field is rotated in the xz plane. The black region on the right sides of both panels originates from the localization of the wave function far away from the bottom gate, in the region where the SO coupling is weak. This is apparent in Fig. 9, which shows the squared wave function for $k_z = 0.4$ nm^{-1} under different magnetic field orientations.

Interestingly, we observe unusual behavior in the region where $\langle g_{\rm SO}^{xx}\rangle$ changes sign. As discussed earlier, when the magnetic field is directed along the x axis, this sign change is due to a subband crossing. However, here the finite z component of the magnetic field, perpendicular to the effective Rashba field, causes anticrossing of the subbands. The magnitude and position of the anticrossing in wave vector space depend on the orientation of **B**. The behavior of $\langle g_{\rm SO}^{xx}\rangle$ damping to zero at the sign change region, accompanied by a maximum in $|\langle g_{\rm SO}^{zz}\rangle|$, can be explained by considering the evolution of electron spin at the anticrossing. Figure 10 presents the z-spin polarization of the lowest subbands, defined as $P = \int(|\psi_{k_z}^{\uparrow}(x,y)|^2 - |\psi_{k_z}^{\downarrow}(x,y)|^2)dxdy$, as a function of k_z for

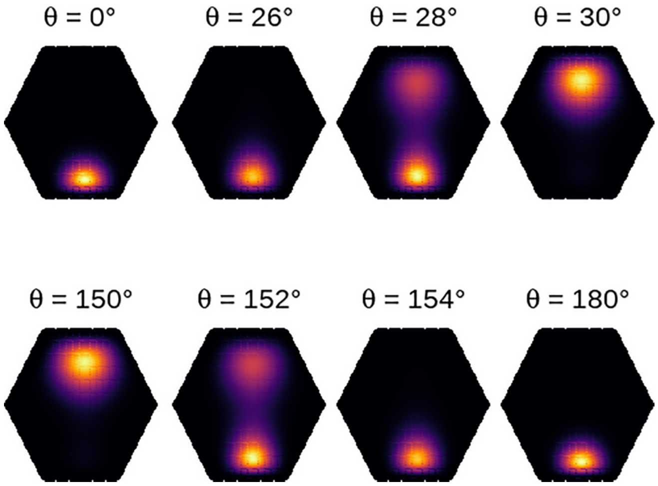

FIG. 9. Squared envelope functions of the lowest subband for $k_z = 0.4$ nm^{-1} as a function of θ at $\varphi = 0$—rotation in the xz plane. Note that the change of the wave function localization from the bottom to the top facet is quite abrupt and happens over an interval of $\approx 4^\circ$.

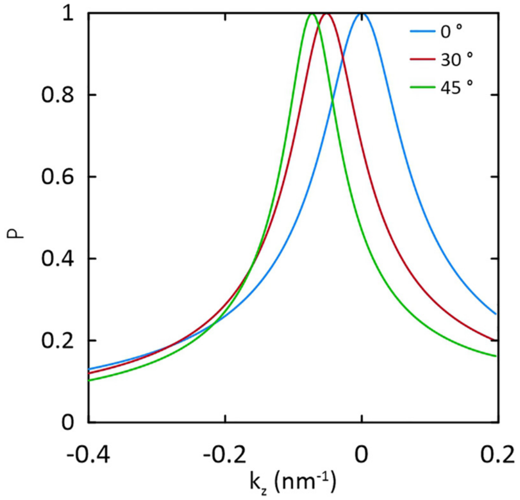

FIG. 10. Spin polarization P as a function of wave vector k_z for the lowest subbands as a magnetic field $B = 1$ T is rotated in the xz plane, at selected angles (see legend).

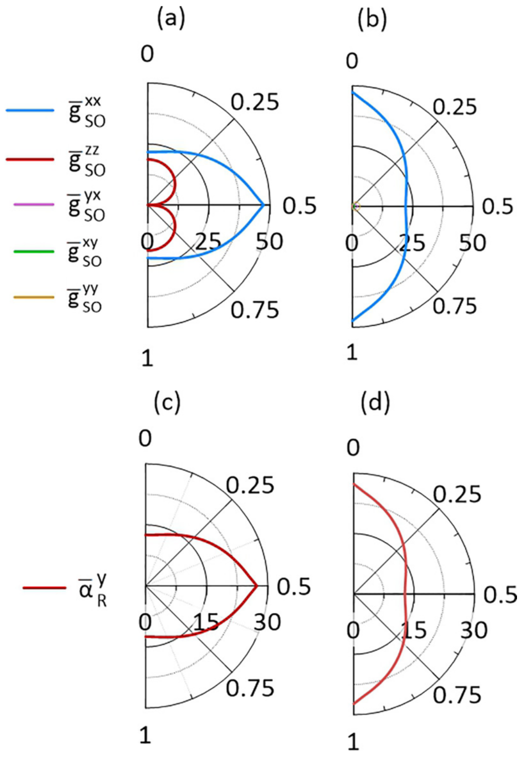

FIG. 11. Averaged Landé tensor elements $\overline{g}^{ab}_{\mathrm{SO}}$ and the Rasha SO constant $\overline{\alpha}^{y}_{R}$ for the magnetic field rotated in two rotation planes [(a) and (c)] xz and [(b) and (d)] xy. Results for the bottom gate potential $V_g = 0.2$ V and magnetic field $B = 1$ T.

different angles, θ. We observe that at the anticrossing, the states become completely z-spin polarized, which maximizes $|\langle g^{zz}_{\mathrm{SO}}\rangle|$. Simultaneously, the average value of σ_x, which determines $|\langle g^{xx}_{\mathrm{SO}}\rangle|$ [see Eq. (23a)], becomes zero, which explains its vanishing for a specific k_z vector.

The evolution of the SO-induced Landé factor in the xy rotation planes, the second for which we observe two fold anisotropy and depicted in Figs. 8(c)–8(f), is in general a result of the interplay between the wave-function localization, which is determined by orbital effects, and the electron spin direction, which is defined by both the SO interaction and the external magnetic field. It is worth noting that when the magnetic field has a component along the y axis, the off-diagonal elements of the $\mathbf{g}_{\mathrm{SO}}$ tensor may also contribute significantly to the effective Landé factor—the magnitudes of $\langle g^{xy(yx)}_{\mathrm{SO}}\rangle$ in Figs. 8(d) and 8(e) are comparable to those of the diagonal elements.

Although the maps of the $\mathbf{g}_{\mathrm{SO}}$ tensor elements presented so far provide valuable information and offer a precise representation of the physical phenomena underlying the anisotropy of g^*, it becomes challenging to directly compare them with results of recent experimental evidence. In experiments, the k_z vector is often not well-defined, and what is typically obtained is an average value of g^* over all electronic states involved in the transport. For this reason, we define the mean value of $\mathbf{g}_{\mathrm{SO}}$ tensor elements averaged over all occupied states

$$\overline{g}^{ab}_{\mathrm{SO}} = \frac{\sum_{k_z} |\langle g^{ab}_{\mathrm{SO}}(k_z)\rangle| f(E_{n=1,k_z} - \mu, T)}{\sum_{k_z} f(E_{n=1,k_z} - \mu, T)}, \qquad (28)$$

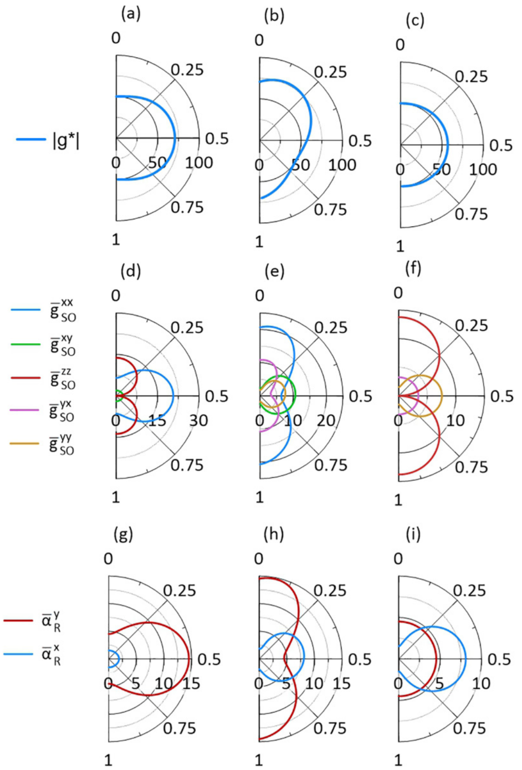

FIG. 12. g^* [Eq. (16)], Landé tensor elements $\overline{g}^{ab}_{\mathrm{SO}}$ and the Rasha SO constant $\overline{\alpha}^{x(y)}_{R}$ for the magnetic field rotated in three rotation planes [(a), (d), and (g)] xz, [(b), (e), and (h)] xy, and [(c), (f), and (i)] yz. Results for the gate configuration with the attached top and left-top gate and $V_g = 0.2$ V and magnetic field $B = 1$ T.

where $a, b = \{x, y, z\}$. Such an approach has been recently used for analyzing the SO coupling in NWs and good agreement with experiments has been obtained [19].

In Fig. 11, we show the mean value of the tensor elements $\overline{g}^{ab}_{\mathrm{SO}}$ and the Rashba SO constant $\overline{\alpha}^{y}_{R}$ (defined in the same manner) for the rotation planes xz and xy characterizing by the twofold anisotropy of g^*. We observe that irrespective of the rotation plane, all elements $\overline{g}^{ab}_{\mathrm{SO}}$ exhibit strong anisotropy with a twofold symmetry, closely corresponding to the evolution of the SO coupling, shown in Figs. 11(c) and 11(d) (with a bottom gate $\overline{\alpha}^{x}_{R} = 0$ due to the symmetry along the y axis and it is not shown). A similar twofold symmetry with respect to the magnetic field direction has been recently observed in the Rashba SO coupling measured for suspended InAs NW [52]. In both cases, the symmetry arises from the bottom gate architecture, which induces a large SO coupling near the bottom facet, while the rotating magnetic field alters localization of the wave function, due to the orbital effects.

It is noteworthy that $\overline{g}^{xx}_{\mathrm{SO}}$ remains the most robust against the rotation in the xy plane [see Fig. 11(b)], and it dominates over other terms for the considered gate setup. This can be attributed to the large coupling constant $\overline{\alpha}^{y}_{R}$ induced by the bottom gate voltage and the broken symmetry with respect to the x axis—see Eq. (21a). Finally, it should be emphasized that the off-diagonal tensor components are one order of magnitude smaller than the diagonal ones. This observation holds true for the considered bottom gate configuration, which

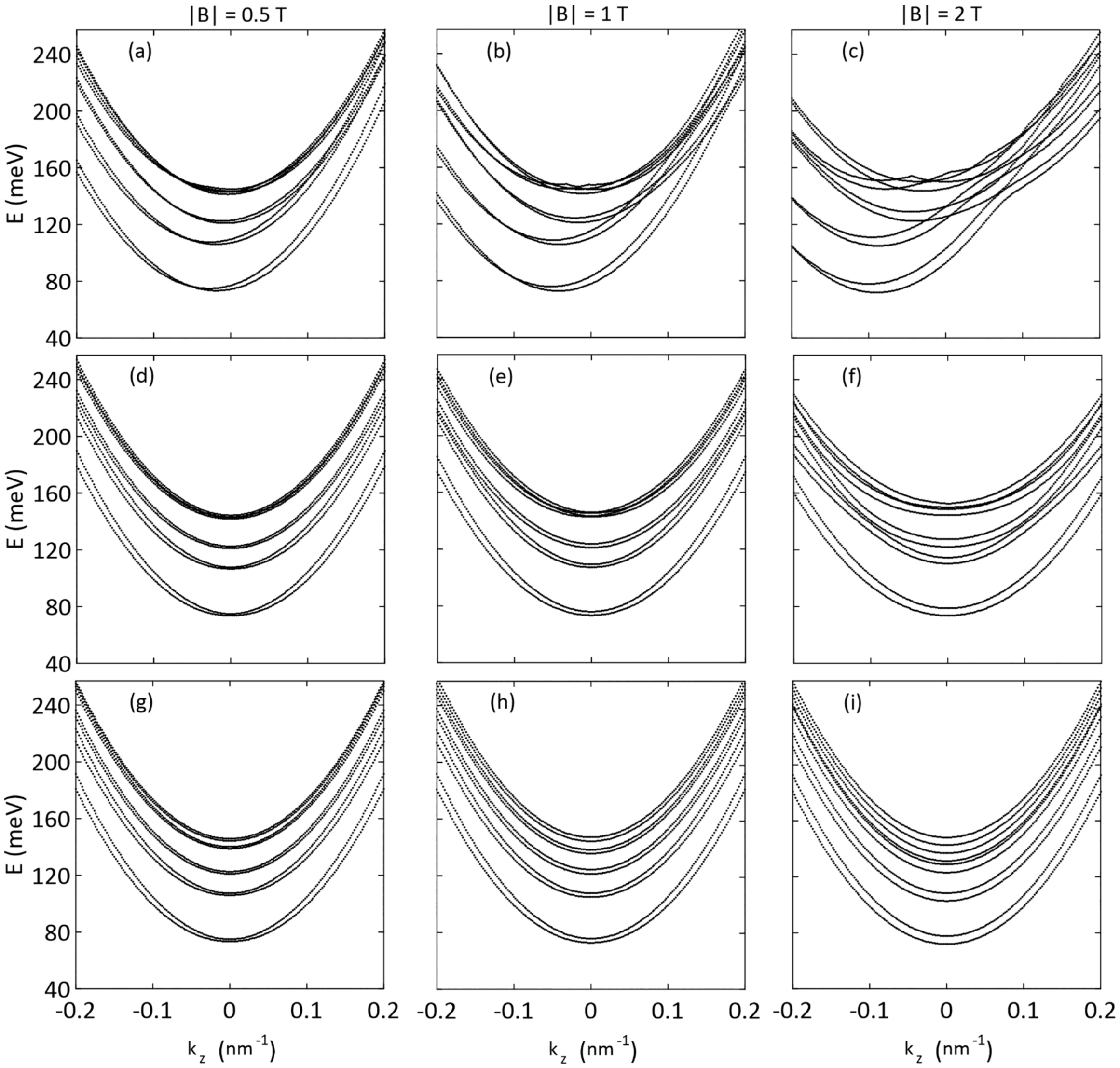

FIG. 13. Dispersion relations $E(k_z)$ for ten lowest energy levels. Individual rows correspond to magnetic field directed along x [(a)–(c)], y [(d)–(f)], and z [(g)–(i)] axes, respectively. Each column corresponds to the magnetic field magnitude: $|B| = 0.5$ [(a), (d), and (g)], 11 [(b), (e), and (h)], and 2 T [(c), (f), and (i)].

preserves symmetry around the y axis, but it may differ for more sophisticated gate configurations as presented in the next section.

C. Different gate configuration

In order to analyze in detail the magnitude of the off-diagonal elements of the $\mathbf{g}_{\mathrm{SO}}$ tensor let us now consider an asymmetric gate configuration with two gates attached to the top and left-top facet. In this case the voltage applied to the gates generate both the x and y component of the Rashba SO coupling—see Figs. 12(g)–12(i). In particular, the negative voltage generates the effective band bending near the gates similar to that observed in the Majorana NWs at the superconductor/semiconductor interface [44].

The g^* factor at $k_z = 0$ is presented in Figs. 12(a)–12(c). We see an enhancement of g^* with respect to g_{RLZ} when the magnetic field is rotated in the xz and xy plane, with strong anisotropy determined by the gate configuration. As shown in Fig. 12(d), in this configuration, the off-diagonal elements of $\mathbf{g}_{\mathrm{SO}}$ are of the same order of magnitude as the diagonal elements. This additional contribution plays a role in enhancing the overall effective Landé factor. While the general principle that the largest SO-induced Landé factor occurs when the magnetic field is perpendicular to $\boldsymbol{\alpha}_R$ is observed also for this gate configuration. Consequently, we believe that our model, when applied to higher gate voltages, can account for the observed twofold enhancement of the effective Landé factor, as recently observed in Majorana NWs [7,43,44].

IV. SUMMARY

Based on the $\mathbf{k} \cdot \mathbf{p}$ theory within the envelope function approximation, we have analyzed the effective Landé factor induced by the SO coupling in homogeneous semiconductor NWs under different magnetic field and gate configurations. By considering the orbital effects in the kinetic and SO terms, we have obtained the $\mathbf{g}_{\mathrm{SO}}$ tensor which is treated as an

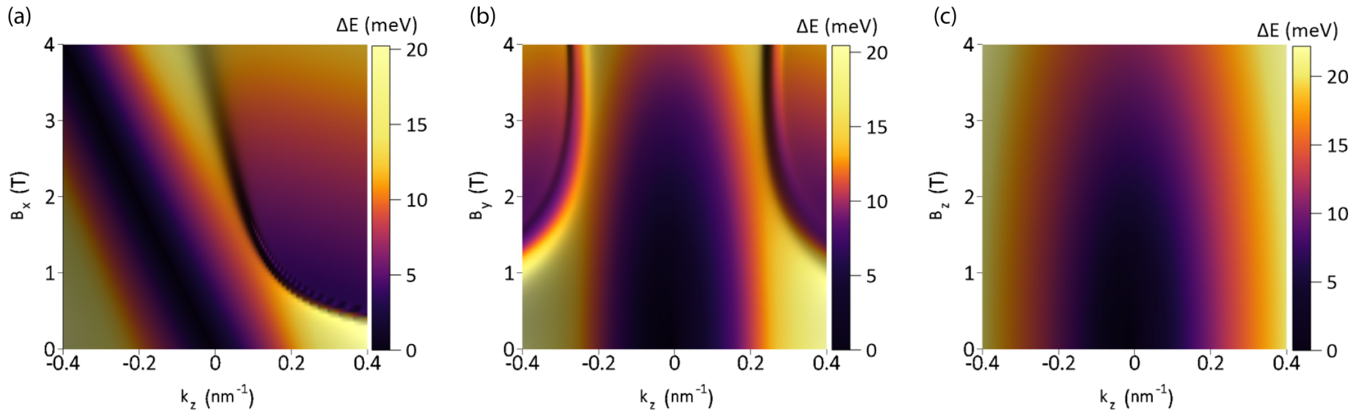

FIG. 14. The energy difference between the first excited and ground state ΔE as a function of wave vector k_z and the magnetic field applied along (a) x, (b) y, and (c) z axes. Results for $V_g = 0.2$ V.

auxiliary quantity to analyze the magnetic field dependence of g^*. In the paper, we have studied the Landé factor as well as the matrix elements of $\mathbf{g}^*_{\mathrm{SO}}$ with respect to the magnetic field magnitude and orientation.

We show that individual elements of the effective Landé tensor induced by SO interaction are proportional to the Rashba coupling constant, which arises from the electric field generated by the adjacent gates. Hence, we have found that g^* is determined by two factors: (1) position and symmetry of the electron's wave function, which can be tuned by the orbital effects, and (2) the spin polarization of the electronic state. Specifically, when we apply the magnetic field perpendicular to NW, the inversion symmetry of the envelope functions is broken and the wave function is squeezed to the NW surface by a k_z-dependent effective potential. This effect results in an enhancement of g^* in a situation when the envelope function is squeezed to the facet near the gate where the electric field and consequently the Rashba SO coupling is larger. The opposite magnetic field (or k_z) results in the squeezing of wave function to the opposite facet where electric field from the gate and the corresponding SO coupling is weak, which results in nearly zero $\mathbf{g}_{\mathrm{SO}}$ and $g^* = g_{\mathrm{RLZ}}$. On the other hand, for **B** directed along the NW axis the orbital effects are strongly reduced by the confinement and g^* as well as $\mathbf{g}_{\mathrm{SO}}$ depends on the z component of spin polarization, which is a resultant of the magnetic and effective Rashba field. Our results explains the recently demonstrated enhancement of the effective Landé factor observed in semiconductor NWs as well as its anisotropy [7,43,44].

Note that although our simulations have been limited to the regime where only the lowest subband is occupied, from our previous papers we expect that the electron-electron interaction, here introduced at the mean-field level, could be essential in estimating Landé factor, via charge localization. At the high concentration regime total energy is minimized by reducing repulsive Coulomb energy, moving electrons outwards, and charge localizes at the six quasi-1D channels at the edges. As we discussed in Ref. [18], this strong localization is almost insensitive to the gate potential and the magnetic field direction.

Finally, we would like to underline that our model does not include the hole bands coupling expressed in the $\mathbf{k} \cdot \mathbf{p}$ model by the Lüttinger parameters [48]. Note however, that as recently shown in Ref. [19] the applied conduction band approximation underestimates the SO coupling constant for the considered zinc-blende crystal structure. As the considered SO induced Landé factor depends on the Rashba SO constants, we expect that the renormalization of the effective g^* observed in the experiments should be even greater than predicted by our results.

ACKNOWLEDGMENTS

We gratefully acknowledge Polish high-performance computing infrastructure PLGrid (HPC Centers: ACK Cyfronet AGH) for providing computer facilities and support within computational Grant No. PLG/2022/015712.

APPENDIX A: DISPERSION RELATIONS

In the paper, we have presented mainly g^*, defined as the proportionality factor of the linear response of electronic states to the magnetic field. For completeness, the full dispersion relations $E(k_z)$ of the nanowire, including the interaction with magnetic field as well as the Rashba SO coupling, are presented in Fig. 13, for chosen magnetic field magnitudes and directions. The corresponding maps presenting the energy difference between the first excited and ground state ΔE are presented in Fig. 14.

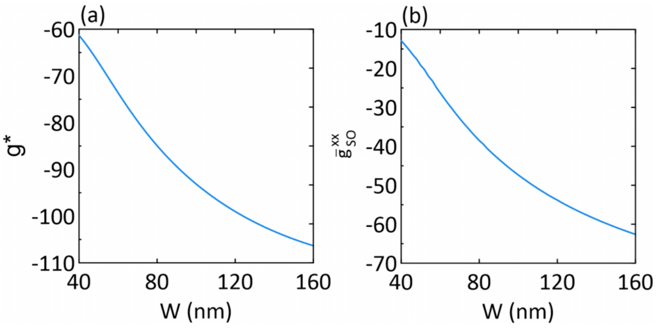

FIG. 15. (a) g^* [Eq. (16)] and (b) averaged $\bar{g}^{xx}_{\mathrm{SO}}$ as a function of the NW width. Calculations for the magnetic field applied along x direction, $B_x = 0.1$ T and $V_g = 0.2$ V.

APPENDIX B: SIZE DEPENDENCE

Calculations presented in the paper have been carried out for the NW width $W = 100$ nm for two reasons. First, it is a typical diameter of NWs fabricated by the commonly used fabrication methods and second, for this range of NW width, orbital effects considered here become significant. For completeness, in Fig. 15, we present $g^*(k_z = 0)$ and $\bar{g}_{\mathrm{SO}}^{xx}$ calculated with a magnetic field along the x directions for which we observe the enhancement of the effective Landé factor. As expected, for a small diameter, when the orbital effect are highly reduced, the SO induced Landé factor approaches zero, which shows that the predicted enhancement of g^* is observable only for NWs of moderate or large width.

[1] M. E. Reimer, M. P. van Kouwen, M. Barkelind, M. Hocevar, M. H. M. van Weert, R. E. Algra, E. P. A. M. Bakkers, M. T. Björk, H. Schmid, H. Riel, L. P. Kouwenhoven, and V. Zwiller, J. Nanophoton. **5**, 053502 (2011).

[2] T. Stettner, P. Zimmermann, B. Loitsch, M. Döblinger, A. Regler, B. Mayer, J. Winnerl, S. Matich, H. Riedl, M. Kaniber, G. Abstreiter, G. Koblmüller, and J. J. Finley, Appl. Phys. Lett. **108**, 011108 (2016).

[3] Y. Li, F. Qian, J. Xiang, and C. M. Lieber, Mater. Today **9**, 18 (2006).

[4] J. A. Czaban, D. A. Thompson, and R. R. LaPierre, Nano Lett. **9**, 148 (2009).

[5] S. Nadj-Perge, S. M. Frolov, E. P. A. M. Bakkers, and L. P. Kouwenhoven, Nature (London) **468**, 1084 (2010).

[6] S. M. Frolov, S. R. Plissard, S. Nadj-Perge, L. P. Kouwenhoven, and E. P. A. M. Bakkers, MRS Bull. **38**, 809 (2013).

[7] M. D. Schroer, K. D. Petersson, M. Jung, and J. R. Petta, Phys. Rev. Lett. **107**, 176811 (2011).

[8] V. S. Pribiag, S. Nadj-Perge, S. M. Frolov, J. W. G. van den Berg, I. van Weperen, S. R. Plissard, E. P. A. M. Bakkers, and L. P. Kouwenhoven, Nat. Nanotechnol. **8**, 170 (2013).

[9] S. Miladić, P. Stipsić, E. Dobardžić, and M. Milivojević, Phys. Rev. B **101**, 155307 (2020).

[10] S. Nadj-Perge, V. S. Pribiag, J. W. G. van den Berg, K. Zuo, S. R. Plissard, E. P. A. M. Bakkers, S. M. Frolov, and L. P. Kouwenhoven, Phys. Rev. Lett. **108**, 166801 (2012).

[11] P. Wójcik, J. Adamowski, B. J. Spisak, and M. Wołoszyn, J. Appl. Phys. **115**, 104310 (2014).

[12] G. Dresselhaus, Phys. Rev. **100**, 580 (1955).

[13] Yu. A. Bychkov and E. I. Rashba, JETP Lett. **39**, 78 (1984).

[14] T. Campos, P. E. Faria Junior, M. Gmitra, G. M. Sipahi, and J. Fabian, Phys. Rev. B **97**, 245402 (2018).

[15] I. A. Kokurin, Physica E **74**, 264 (2015).

[16] I. A. Kokurin, Solid State. Commun. **195**, 49 (2014).

[17] P. Wójcik, A. Bertoni, and G. Goldoni, Phys. Rev. B **97**, 165401 (2018).

[18] P. Wójcik, A. Bertoni, and G. Goldoni, Phys. Rev. B **103**, 085434 (2021).

[19] S. D. Escribano, A. L. Yeyati, and E. Prada, Phys. Rev. Res. **2**, 033264 (2020).

[20] P. Wójcik, A. Bertoni, and G. Goldoni, Appl. Phys. Lett. **114**, 073102 (2019).

[21] S. Furthmeier, F. Dirnberger, M. Gmitra, A. Bayer, M. Forsch, J. Hubmann, C. Schüller, E. Reiger, J. Fabian, T. Korn, and D. Bougeard, Nat. Commun. **7**, 12413 (2016).

[22] I. van Weperen, B. Tarasinski, D. Eeltink, V. S. Pribiag, S. R. Plissard, E. P. A. M. Bakkers, L. P. Kouwenhoven, and M. Wimmer, Phys. Rev. B **91**, 201413(R) (2015).

[23] J. Kammhuber, M. C. Cassidy, F. Pei, M. P. Nowak, A. Vuik, Ö. Gül, D. Car, S. R. Plissard, E. P. A. M. Bakkers, M. Wimmer, and L. P. Kouwenhoven, Nat. Commun. **8**, 478 (2017).

[24] S. Dhara, H. S. Solanki, V. Singh, A. Narayanan, P. Chaudhari, M. Gokhale, A. Bhattacharya, and M. M. Deshmukh, Phys. Rev. B **79**, 121311(R) (2009).

[25] Z. Scherübl, G. Fülöp, M. H. Madsen, J. Nygård, and S. Csonka, Phys. Rev. B **94**, 035444 (2016).

[26] D. Liang and X. P. A. Gao, Nano Lett. **12**, 3263 (2012).

[27] S. Gazibegovic, D. Car, H. Zhang, S. C. Balk, J. A. Logan, M. W. A. de Moor, M. C. Cassidy, R. Schmits, D. Xu, G. Wang, P. Krogstrup, R. L. M. Op het Veld, K. Zuo, Y. Vos, J. Shen, D. Bouman, B. Shojaei, D. Pennachio, J. S. Lee, P. J. van Veldhoven *et al.*, Nature (London) **548**, 434 (2017).

[28] P. Krogstrup, N. L. B. Ziino, W. Chang, S. M. Albrecht, M. H. Madsen, E. Johnson, J. Nygård, C. M. Marcus, and T. S. Jespersen, Nat. Mater. **14**, 400 (2015).

[29] W. Chang, S. M. Albrecht, T. S. Jespersen, F. Kuemmeth, P. Krogstrup, J. Nygård, and C. M. Marcus, Nat. Nanotechnol. **10**, 232 (2015).

[30] M. Kjaergaard, F. Nichele, H. J. Suominen, M. P. Nowak, M. Wimmer, A. R. Akhmerov, J. A. Folk, K. Flensberg, J. Shabani, C. J. Palmstrøm, and C. M. Marcus, Nat. Commun. **7**, 12841 (2016).

[31] V. Mourik, K. Zuo, S. M. Frolov, S. R. Plissard, E. P. A. M. Bakkers, and L. P. Kouwenhoven, Science **336**, 1003 (2012).

[32] M. T. Deng, C. L. Yu, G. Y. Huang, M. Larsson, P. Caroff, and H. Q. Xu, Nano Lett. **12**, 6414 (2012).

[33] S. M. Albrecht, A. P. Higginbotham, M. Madsen, F. Kuemmeth, T. S. Jespersen, J. Nygård, P. Krogstrup, and C. M. Marcus, Nature (London) **531**, 206 (2016).

[34] H. Zhang, C.-X. Liu, S. Gazibegovic, D. Xu, J. A. Logan, G. Wang, N. van Loo, J. D. S. Bommer, M. W. A. de Moor, D. Car, R. L. M. Op het Veld, P. J. van Veldhoven, S. Koelling, M. A. Verheijen, M. Pendharkar, D. J. Pennachio, B. Shojaei, J. S. Lee, C. J. Palmstrøm, E. P. A. M. Bakkers *et al.*, Nature (London) **556**, 74 (2018).

[35] A. D. K. Finck, D. J. Van Harlingen, P. K. Mohseni, K. Jung, and X. Li, Phys. Rev. Lett. **110**, 126406 (2013).

[36] Y. Oreg, G. Refael, and F. von Oppen, Phys. Rev. Lett. **105**, 177002 (2010).

[37] J. D. Sau, R. M. Lutchyn, S. Tewari, and S. Das Sarma, Phys. Rev. Lett. **104**, 040502 (2010).

[38] R. M. Lutchyn, J. D. Sau, and S. Das Sarma, Phys. Rev. Lett. **105**, 077001 (2010).

[39] L. Roth, B. Lax, and S. Zwerdling, Phys. Rev. **114**, 90 (1959).

[40] G. Lommer, F. Malcher, and U. Rössler, Phys. Rev. B **32**, 6965(R) (1985).

[41] A. A. Kiselev, E. L. Ivchenko, and U. Rössler, Phys. Rev. B **58**, 16353 (1998).

[42] K. Gawarecki and M. Zieliński, Sci. Rep. **10**, 22001 (2020).

[43] I. van Weperen, S. R. Plissard, E. P. A. M. Bakkers, S. M. Frolov, and L. P. Kouwenhoven, Nano Lett. **13**, 387 (2013).

[44] S. Vaitiekėnas, M.-T. Deng, J. Nygård, P. Krogstrup, and C. M. Marcus, Phys. Rev. Lett. **121**, 037703 (2018).

[45] G. W. Winkler, D. Varjas, R. Skolasinski, A. A. Soluyanov, M. Troyer, and M. Wimmer, Phys. Rev. Lett. **119**, 037701 (2017).

[46] R. Lassnig, Phys. Rev. B **31**, 8076 (1985).

[47] A. Bertoni, M. Royo, F. Mahawish, and G. Goldoni, Phys. Rev. B **84**, 205323 (2011).

[48] A. Vezzosi, A. Bertoni, and G. Goldoni, Phys. Rev. B **105**, 245303 (2022).

[49] B. D. Woods, T. D. Stanescu, and S. Das Sarma, Phys. Rev. B **98**, 035428 (2018).

[50] F. Stern, Phys. Rev. B **5**, 4891 (1972).

[51] T. Ando, Phys. Rev. B **13**, 3468 (1976).

[52] A. Iorio, M. Rocci, L. Bours, M. Carrega, V. Zannier, L. Sorba, S. Roddaro, F. Giazotto, and E. Strambini, Nano Lett. **19**, 652 (2019).